Towards behavior by design: A case study on corrugated architectures

E. Plancher, L. Héraud, Pierre Lhuissier, R. Dendievel, D. Fabregue, J.-J. Blandin, G. Martin

Towards behavior by design:
a case study on corrugated architectures.

E. Plancher[1,*], L. Heraud[1], P. Lhuissier[1], R. Dendievel[1],
D. Fabrègue[2], J.-J. Blandin[1], G. Martin[1,*].

1 Université Grenoble Alpes, CNRS UMR5266, Grenoble INP, Laboratoire SIMaP, 38000 Grenoble, France.
2 INSA Lyon, CNRS UMR5510, Laboratoire MATEIS, 69621 Villeurbanne, France.
*corresponding authors: guilhem.martin@simap.grenoble-inp.fr (G. Martin), emeric.plancher@mines-saint-etienne.org (E. Plancher)

Abstract

A design strategy, referred to as *behavior by design*, was introduced to develop novel architectured materials starting from their expected stress-strain response. Target behaviors in this strategy have unusual shapes that provide new functions to the material. Here, a numerical toolbox was employed to predict the geometry of metal tensile samples with a corrugated gauge section, given the expected characteristics of their stress-strain response. A multiscale approach, based on a finite element model, was used to construct characteristic points and indices on the macroscopic stress-strain curves to select the relevant input geometrical parameters. Additive manufacturing (electron beam melting) was employed to build several predicted geometries in Ti-6Al-4V titanium alloy. Mechanical testing revealed a good agreement between the experimental and predicted behaviors with limited difference in strain (0.8 %) and stress (50 MPa). Shape variations such as local thickness fluctuations were identified using X-ray tomography as a source of mismatch between simulations and experiments. The ability to control the whole shape of unusual stress-strain curves is expected to bring new exciting functionalities to architectured materials.

Graphical abstract

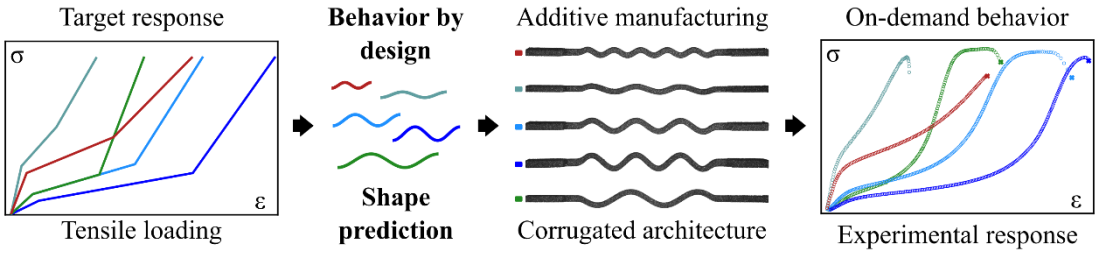

Highlights

- A *behavior by design* strategy was used to develop architectured material with custom mechanical responses.
- A numerical toolbox was established to select input geometrical parameters for corrugated architectures given their expected mechanical behavior.
- Additive manufacturing was employed to build corrugated tensile samples with Ti-6Al-4V titanium alloy.
- Mechanical testing revealed a good agreement between experiments and simulations

Keywords

Behavior by design; additive manufacturing; architectured materials; strain hardening; X-ray tomography;

1. Introduction

Novel metallic materials obtained through recent design strategies can often be described with the concept of *material by design* [1]. Materials by design are developed to reach a given set of properties which is difficult to obtain in their conventional counterparts (*e.g.* high strength & ductility, high strength & toughness, low density & high stiffness). Generally, they are engineered with the support of a modelling approach with the concern to better use their mechanical potential. Most of the time, materials by design can also sustain multiple loadings and fulfill several functions (mechanical, thermal, electrical, etc.).

Conventionally, microstructure enhancement has been the main route towards advanced materials, with the development of multi-phase microstructures, the use of strain-induced phase transformation and twinning. For example, strength-ductility and strength-toughness trade-offs have been improved recently with this approach in several alloy systems such as TRIP-maraging steel [2], QP steel [3], metastable β-titanium alloys [4] and high entropy alloys [5].

In the last decade, however, architectured materials have appeared as a key tool to design materials with unreached sets of properties such as low-density and high-stiffness [1,6]. Additive manufacturing [7] has supported the growing interest in architectured materials by providing reliable tools to manufacture parts with complex geometries, and hollow objects with precise internal features. In single-material architectures, several shape-driven (geometrical) mechanisms have been designed to control levels of properties with little constraints stemming from the manufacturing process. For example, design strategies based on shape optimization have been used to obtain lattice structures with unusual properties (see e.g. the review [8]) and improved energy absorption [9].

Here, we suggest a new design approach, referred to as *behavior by design,* which aims to invent novel architectured materials starting from their expected stress-strain response. The target stress-strain behavior, in this case, has an unusual shape that provides new functions to the material such as differential strain hardening. In general, the interaction between geometrical (architectural) effects and microstructural mechanisms during deformation have to be controlled to generate a complex behavior. As a proof-of concept, a geometrical effect is investigated later, by choosing a situation where homogeneous microstructures with limited strain hardening are considered. The objective of obtaining complex behaviors makes a significant difference from the *material by design* approach where

combinations of properties are the main target, not the shape of the whole stress-strain curve.

In this work, metal tensile specimens with a corrugated gauge are selected as a case study to illustrate the *behavior by design* strategy. Bouaziz *et al.* [10] have shown that sinusoidal corrugations could present an interesting stress-strain response in tension (see Figure 1), starting with a low-stress plateau followed by a peak of strain hardening. The peak of strain hardening originates from a geometrical effect which is triggered when the deformation of the specimen shifts from a mode dominated by the unbending of the corrugation towards the stretching of the straighten sample. Compared to bulk materials, significant localized plasticity occurs in the sample before the whole material deforms and the position of the hardening peak can be modified by changing the geometrical parameters of the corrugation. Fraser *et al.* [11] showed that the general shape of a few stress-strain curves obtained on interstitial-free steel (mechanically shaped into a corrugated geometry) could be predicted with an efficient analytical model. As seen in later results [12], analytical predictions also match finite element simulations but with local deviation of 3-10 % strain. In this work, having access to local stress-strain paths in specific positions of the sample is essential and therefore finite element modelling was selected as it provides an easy way to monitor local loading conditions, at the element scale. Corrugated architectures have been employed as reinforcements in metal-metal composite materials [12] and can be envisioned as improved energy-absorbing materials. In the automotive sector for example, an architecture with two stress-plateau (see figure 1) could react passively to a pedestrian impact (at low stress level) and then to a higher impact (at high stress level) with appropriate responses for each scenario.

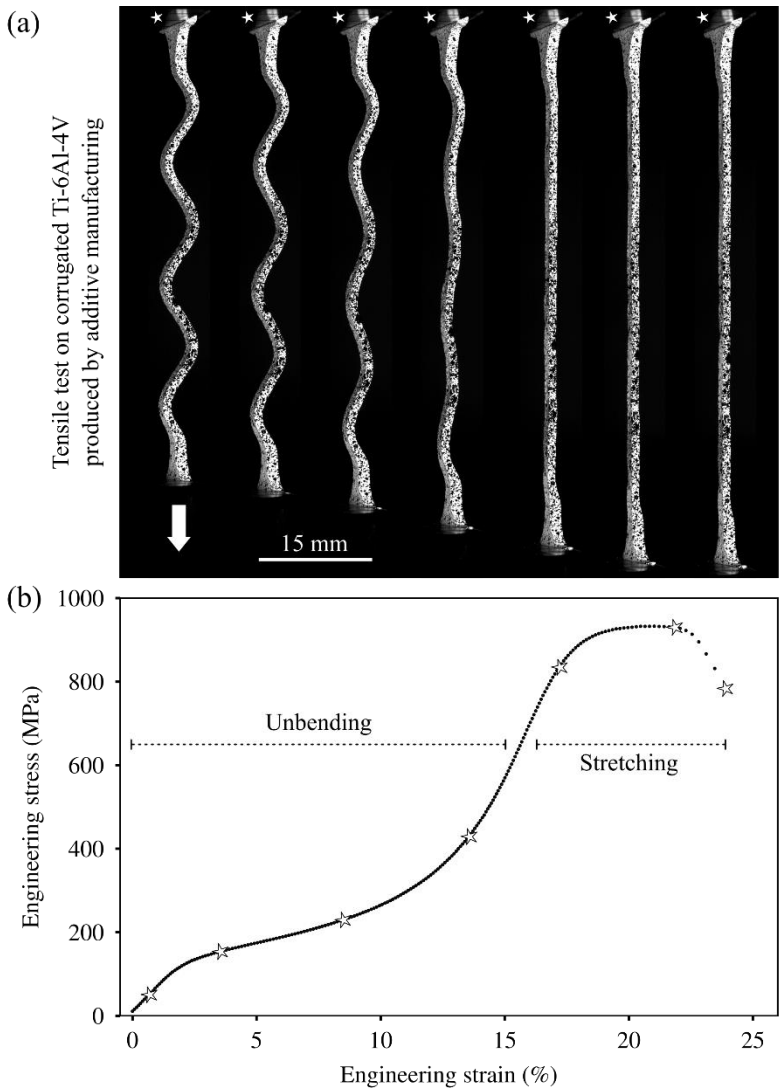

Figure 1. Tensile behavior of a Ti-6Al-4V sample with a corrugated gauge produced by additive manufacturing. (a). Optical images illustrating two deformation modes, one dominated by the unbending of the corrugation and one dominated by stretching. (b) Equivalent stress-strain curve of the central part of the gauge. White stars indicate the points where the optical images presented in (a) were acquired.

Powder-bed additive manufacturing is the key technology enabling our design strategy to produce a valuable output. An additive manufacturing technique such as electron beam melting allows to construct parts with an accurate complex shape and relatively homogenous mechanical properties, two characteristics difficult to achieve through conventional forming methods. In previous studies, corrugations were obtained by press-forming flat ductile sheet metal between two anvils composed of cylindrical pins [10,12]. The corrugation period was tuned by moving the pins apart and the corrugation amplitude was changed by adjusting the forming pressure. As in every forming operation, forming tools have to be designed accounting for spring back effects and strain paths effects on the material local behavior. Constrains on the forming operation

tend to limit the range of shape available and bring significant amounts of complexity in the design strategy. An additional consequence of using a forming step is to pre-deform and harden the material in a heterogeneous manner, leading to local changes in its mechanical properties.

Titanium alloy Ti-6Al-4V were chosen as a test material to decorrelate the geometrical effect investigated here from potential microstructural effects. On the one hand, this material is well suited to provide initial homogeneous microstructures after additive manufacturing and post-processing heat treatments. Thanks to a texture randomization brought by the $\beta \rightarrow \alpha$ phase transformation during cooling, its mechanical properties can be fairly isotropic. For example, tensile properties of Ti-6Al-4V samples produced by electron beam melting only slightly depend on their orientation during the build [18–20]. Ti-6Al-4V has been used to build architectured objects with a complex shape such as lattices and foams [13–17]. On the other hand, the intrinsic limited work hardening capacity of Ti-6Al-4V is an additional opportunity to decouple geometrical and microstructural effects as its mechanical properties evolve little during deformation.

In what follows, a multi-scale approach was used to identify characteristic features in tensile curves simulated with the finite element method. Criteria were established, considering the stress/strain paths of key elements in the model, to define indices representing the macroscopic behavior. Maps of index values were used to illustrate the direct link established (through a limited set of simulations) between characteristic features of the curves and input geometrical parameters. A selection tool was then employed to predict the geometry of several Ti-6Al-4V samples, without additional simulations, given the expected characteristics of their stress-stain response. To validate the method, several samples have been manufactured by electron beam melting and post-processed accordingly. The agreement between the predicted and the experimental data is discussed and used to comment on the success and limits of the proposed design strategy.

2. Methodology

The present study focuses on tensile specimens with a corrugated gauge along a sinusoidal shape. As illustrated in Figure 2, three parameters are used to describe the geometry of the corrugated part: the period (P), the amplitude of the neutral fiber (h) and the sample thickness (e). The width of the sample (w) is assumed to be of the same order of magnitude as the thickness e. In other words, narrow samples are considered, not sheet metal.

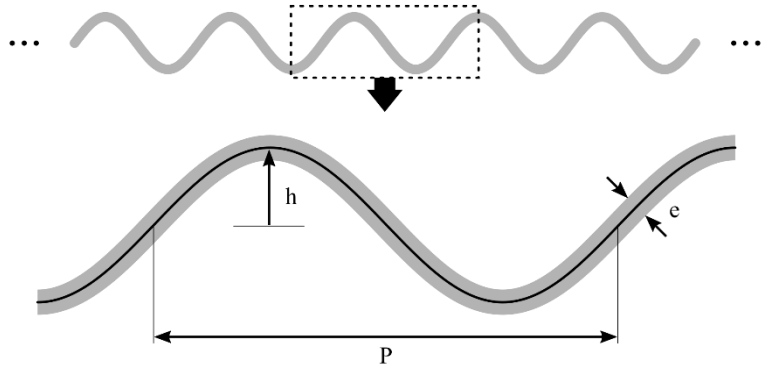

Figure 2. Parameters used to describe a corrugated sample with a sinusoidal shape.

2.1. Finite element framework

Due to the periodic nature of the corrugation, a model for a single period was built with the finite element method (see Figure 3). The *Europlexus* software was used to perform all simulations with a solving algorithm featuring a large-displacement and large-rotation framework. Time integration was achieved through an explicit scheme. Plane stress boundary conditions have been chosen in the 2D model after full 3D calculations were carried out and no clear deviation from the results were observed. Linear quadrangle elements with four integration points were selected to build the mesh. With a mesh sensitivity analysis, it was found that 20 elements along the thickness of the sample provided a stable and consistent solution. Mass scaling was used to speed up the simulations by virtually increasing the material density ($4400\ kg/m^3$) by a factor 10. As the discretization through the thickness was kept constant, the number of elements per simulation depended on the geometry considered: the largest simulation had ~14000 elements and ran in a day on a single CPU while the fastest simulation had ~3000 elements and was completed in about 2 h. For time-efficiency concerns, all simulations have been performed up to 25 % equivalent macroscopic strain.

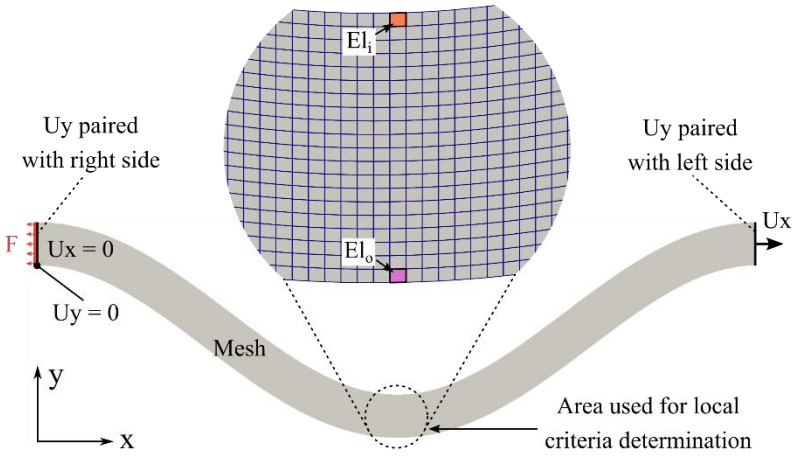

Figure 3. Description of the 2D finite element model. Displacements U_x and U_y are used to control the simulation while the force F is an output. An illustration of the mesh is shown in inset, with two specific elements (El_i and El_o) used later to define characteristic points on the macroscopic stress-strain curves.

A von Mises criterion of plasticity was selected and the experimental stress-strain curve presented in Figure 4 was taken as input for the constitutive behavior. A constant hardening rate was assumed after 8 % strain to represent the behavior present locally in the material after macroscopic necking. The following input parameters were taken to match the experiment: $E = 129\ GPa$ (Young's modulus), $\nu = 0.34$ (Poisson's ratio) and $\sigma_0 = 817\ MPa$ (yield stress). The output force-displacement curve collected from the simulation was transformed in an engineering stress-strain curve, considering the initial sample thickness e and the initial period P. As described below, a method was then developed to represent the macroscopic stress-strain curves with a handful of mathematical indices, based on the definition of characteristic points.

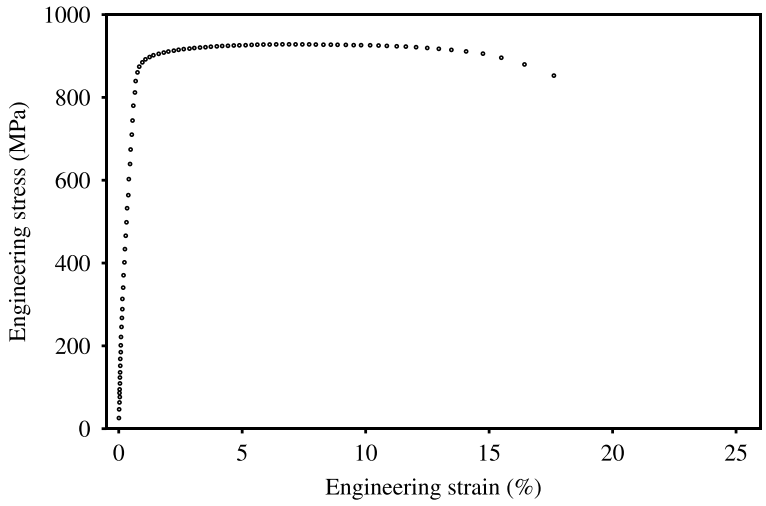

Figure 4. Engineering stress-strain curve obtained on a straight tensile specimen built and post-processed with the corrugated samples used in this study.

2.1.1. Defining characteristic points based on local stress paths

Three characteristic points (P1, P2 and P3) were defined to reflect key deformation steps on the macroscopic stress-strain curves (c.f. Figure 5a). Point P1 indicated the apparent yield of the corrugated sample, P2 was characteristic of the transition between bending-dominated and stretching-dominated deformation while P3 attested of the complete unbending of the sample. To position P1, P2 and P3 in a consistent way, criteria have been established on local stress states.

The local stress state of two elements in the mesh (El_i and El_o) were used to define P1, P2 and P3. The two elements were selected in the bottom part of the corrugation (see Figure 3), in a region prone to stress localization, along a plane of symmetry and spread across the thickness of the sample. As shown in Figure 5b, a uniaxial stress state along the x axis was observed at both locations, a result consistent with a macroscopic loading composed of pure bending and stretching. On the inner side of the corrugation (element El_i), positive tensile stress was always present whereas compressive states were observed on the external side (element El_o). The shift between compressive and tensile stress observed on El_o was correlated with the transition between bending-dominated and stretching deformation modes.

As seen in Figure 5c, El_i was the first element in the sample to yield so P1 was defined on El_i as the point where $\sigma_{xx} = \sigma_{yield}$. The sharp transition in stress state observed on El_o was used to define P2 as the point of the curve where $\partial\sigma_{xx}/\partial\varepsilon = 0$. At P2, El_o was being pulled towards tension as stretching becomes the significant deformation mode. Note that a bending stress field was still present at P2 in the sample. P3 was defined as the point where El_o reaches the initial yield stress in tension, reflecting that the sample had been straightened entirely.

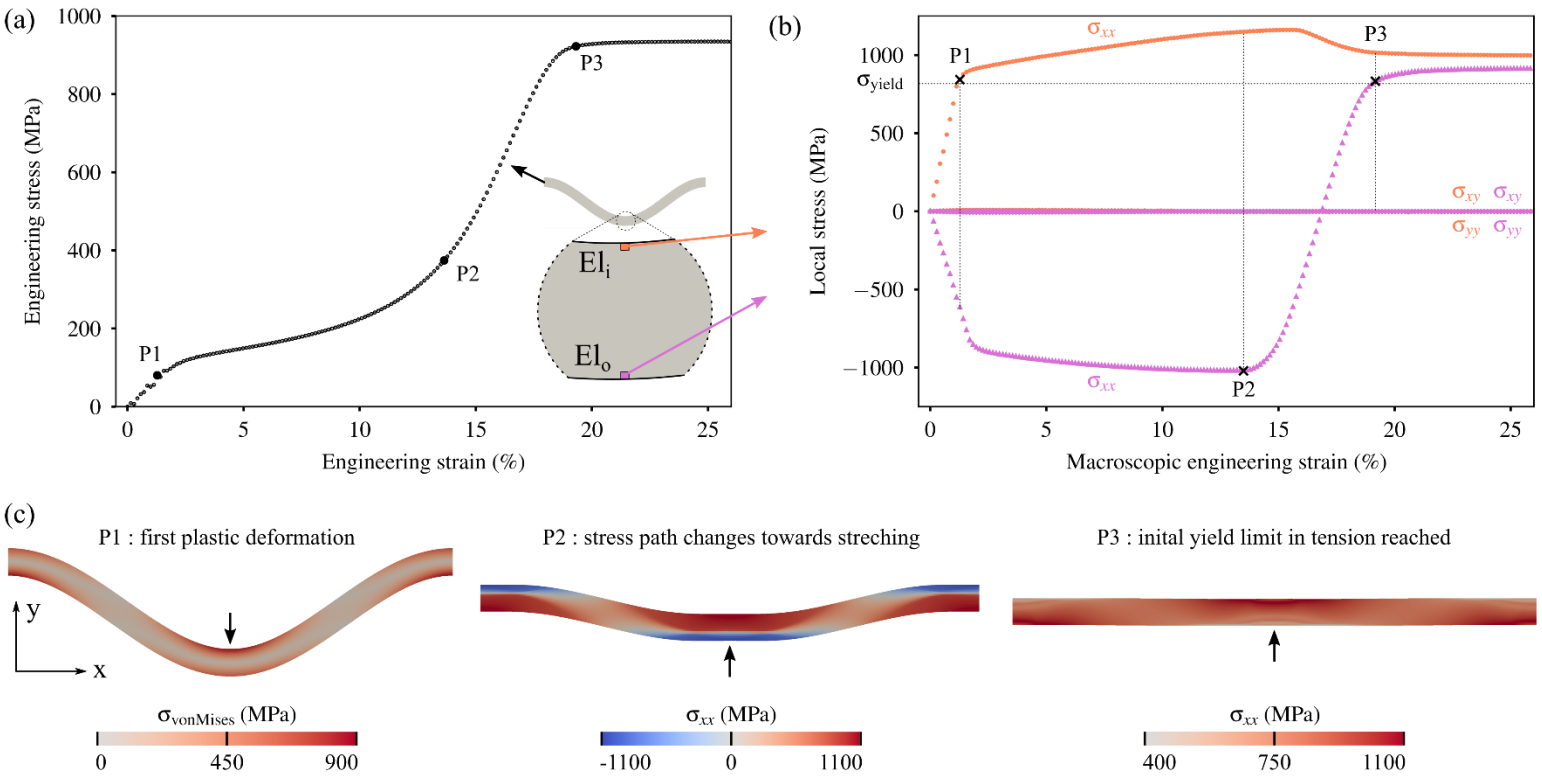

Figure 5. Definition of three characteristic points on the stress-strain curves by considering local stress paths at different locations through the thickness of the corrugated sample. The FE simulation performed with e=1.04 mm, h=2 mm and P=16.7 mm is used as an example. (a) Position of the characteristic points P1, P2 and P3 on the macroscopic stress-strain curve. (b) Local stress states observed at two positions in the corrugation (orange elements El_i and purple element El_o). (c) Stress fields in the sample at P1, P2 and P3. Equivalent von Mises values are used to show the stress localization at P1 while uniaxial component σ_{xx} is used to show the stress gradient present in the bottom part of the corrugation at P2 and P3.

2.1.2. Description of the stress-strain curves with indices

Six indices were selected to describe the shape of a typical stress-strain curve, based on P1, P2 and P3. As shown in Figure 6, a curve can be described schematically by an equivalent Young's modulus ($\bar{E}$), two hardening rates (H_1 and H_2) and the strains at P1 (ε_1), P2 (ε_2) and P3 (ε_3). The choice of those six indices is not unique but was found more convenient to describe the plastic regime than for example the simple position of P1, P2 and P3.

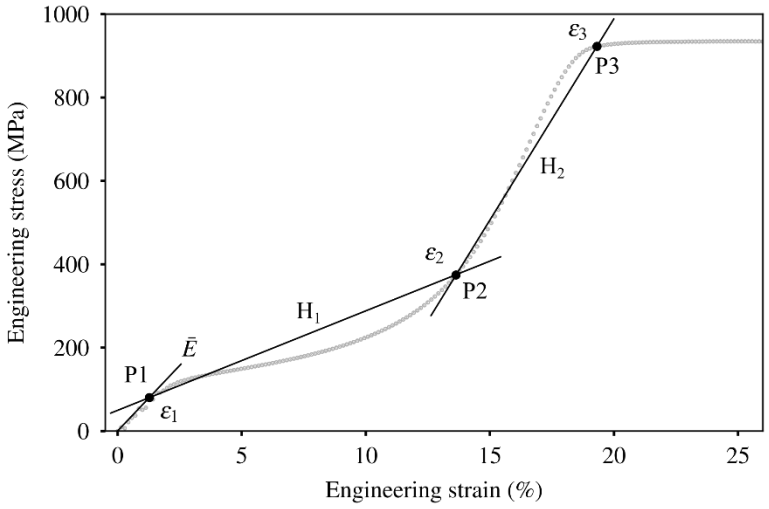

Figure 6. Indices used to describe the simulated stress-strain response of a typical corrugated sample (here: e=1.04 mm, h=2 mm and P=16.7 mm).

To investigate the link between the geometrical parameters of the corrugation (e, h and P) and the value of the descriptive indices ($\bar{E}$, H_1, H_2, ε_1, ε_2 and ε_3), approximately 200 simulations have been performed. The range of thickness investigated was set between 0.75 mm and 1.5 mm. The lower bound was selected considering the ability to manufacture thin parts with the EBM technique. The upper bound was defined from preliminary experiments as the point where most samples break before complete unbending. The range of period P considered was taken between 10 mm and 25 mm, two values linked with the ability to manufacture between 2 and 5 corrugations in a 50 mm-long gauge of typical tensile samples. Amplitudes h between 0.5 mm and 4 mm have been simulated.

2.2. Validation experiments

2.2.1. Production of corrugated tensile samples by EBM

To validate the *behavior by design* strategy, various tensile specimens with a corrugated gauge have been built by electron beam melting (EBM) and further processed with hot isostatic pressing (HIP) and chemical etching.

Commercial Ti-6Al-4V ELI powder was loaded in an A1 EBM machine (Arcam) to produce corrugated tensile specimens. Powder particles were obtained in a spherical shape through plasma atomization with diameters between 45 µm and 100 µm. Their chemical composition, as provided by the manufacturer, is reported in Table 1. All tensile samples were built in a single batch on a 10 mm-thick stainless-steel plate with the sample tensile axis parallel to the build direction. Standard melting parameters were used following the procedure reported in [21]. Every sample was

subsequently subjected to HIP with the goal to eliminate lack-of-fusion type of porosity and to decrease the size of gas-filled spherical pores inherited from the powder [22,23]. The HIP treatment was applied for 2 h at 920 °C in an argon atmosphere pressurized at 1020 Bar and was followed by a slow cooling in the furnace. Chemical etching was finally employed to decrease the number and severity of surface defects such as partially-melted powder particles and plate-pile stacking defects [24–26]. The specimens were immersed at room temperature for 1 h 30 min in a stirred water-based solution containing 12 mL of HF (48 %), 39 mL of HNO_3 (70 %) and 300 mL of deionized water. X-ray tomography (see below) was employed to make sure that no significant internal porosity or plate-pile surface defects were present after post-processing.

Al	V	Fe	C	O	N	H	Y	Ti
6.47	3.98	0.20	0.02	0.08	0.02	0.002	< 0.001	Bal.

Table 1. Chemical composition of the Ti-6Al-4V ELI powder (wt%).

The geometry of all corrugated specimens was adapted from the shape of conventional straight samples with a gauge length $L_0 = 50$ mm, an initial thickness of 2 mm (before etching) and a width of 4 mm (before etching). To perform sound tensile tests, balanced symmetric sample were used with a round number of corrugation (c) along the gauge length. In other words, the samples were designed following the constraint $P = L_0/c$ (with $c = 1, 2, 3 ...$). A straight sample was also built and post-processed similarly to evaluate the material constitutive behavior.

2.2.2. X-ray tomography

X-ray micro-computed tomography (µ-CT) was performed on both a straight sample and a corrugated sample (C3H2) to characterize their geometry and detect any potential internal defect. Helicoidal scans with ~9000 radiographs over 8 turns have been performed in an EASYTOM XL instrument (RX Solutions) with a beam voltage of 150 kV and a voxel size of 6 µm. Reconstruction of the 3D sample was carried out with a filtered back-projection algorithm and further image processing was performed with the FIJI software. A median filter of size 1 was used to reduce noise followed by a straightforward thresholding thanks to the high contrast between the material and air. Finally, a mean distance to the sample sides was calculated over all slices to obtain a precise value of both the sample thickness and width that accounts for an average value of roughness.

2.2.3. Determination of equivalent stress-strain responses

A well-documented issue when calculating stress levels for thin parts produced with EBM is the determination of meaningful cross-section

values [24,27]. Even in etched parts, roughness, surface defects and geometrical variability can reach 150 µm and lead to significant inaccuracy in the definition of the mechanically efficient cross-section. For example, conventional measurements done with a caliper reflects values actually larger than the true cross-section bearing the load. In this work, a down-scaling factor of 0.85 was applied to correct for errors in conventional cross-section measurement. This value was obtained by comparing measurements performed on the straight sample with a caliper (3.1 mm^2) with the average cross-section measured on the same sample by tomography (2.64 mm^2). The scaling factor method is deemed reasonable in this work as surface conditions and approximate cross-section areas are similar from one sample to another.

Tensile tests were performed on a DY 35 tensile machine from ADAMEL equipped with a 20 kN load cell at an equivalent strain rate of $10^{-3}\,s^{-1}$. An optical stereo-correlation system (Aramis GOM) was used to measure the equivalent strain of the central corrugation in each sample to compare with the simulation. The stress-strain curve obtained on a straight sample is shown in Figure 4.

3. Design of corrugated architectures with a custom behavior

In this section, we show how design maps can be constructed and used to predict the geometry of several corrugated samples given their expected stress-strain behavior.

3.1. Simulated behaviors and reliability of the characteristic points.

A variety of behaviors simulated with the finite element model, corresponding to several couples of geometrical input parameters taken among the range being investigated, is illustrated in Figure 7. For stress-strain responses exhibiting a large strain value at P3 (e.g. curves 6, 7 and 8), the curve shape is typical with first a low-stress large-strain plateau, followed by a steep slope associated with a high strain hardening rate, before reaching a high stress plateau close to the ultimate tensile strength of Ti-6Al-4V. In contrast, curves with a low strain value at P3 (typically curve 1) are closer to conventional tensile curves with a relatively high yield stress directly followed by a constant strain hardening rate. Distinct from those two characteristic behaviors, some curves tend to present only an inflexion point that could be considered as an embryo of stress plateau.

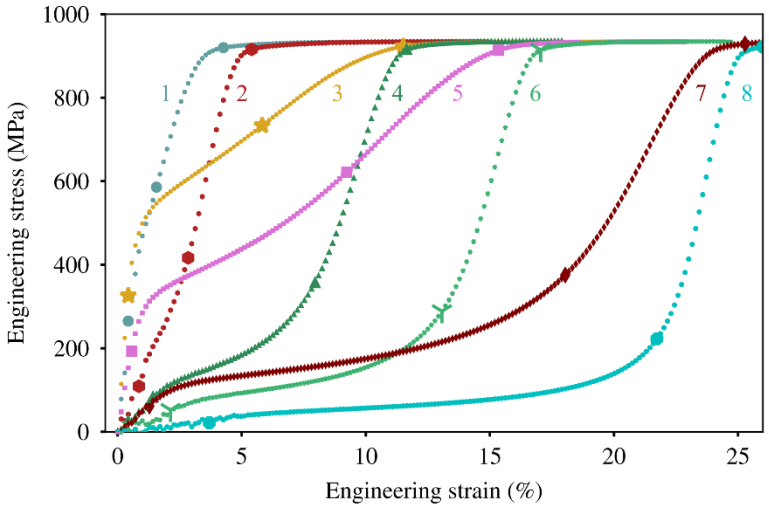

Figure 7. Illustration of the variety of behaviors simulated with several corrugated geometries. Bold symbols represent the position of P1, P2 and P3 as determined by the criteria applied on local stress paths.

The behaviors shown in Figure 7 show promising arguments for the use of corrugated geometries. First, corrugations are an easy way to change the apparent stress-strain response for standard materials. Improvement of apparent properties can be achieved: for example, strain-to-failure can be increased significantly while retaining the ultimate tensile strength of the bulk material. If single properties appear easily tunable (e.g. the apparent stiffness), the ability to control the whole shape of the curve could bring more functionality to the architectured material for example by using the low-stress plateau as a visual sensor of undesirable plastic deformation and the peak of strain hardening as a mechanical safety feature.

As seen in Figure 7, the definition of characteristic points through criteria based on local stress states appears relevant for a large span of behaviors. For all curves, P1 delimits the linear (elastic) portion of the curve and P3 is positioned at the beginning of the high stress plateau. The position of P2 is also very stable: it successfully highlights a diffuse transition between unbending and stretching even when a low-stress plateau is not observed. In Figure 8, characteristic points for all the simulations performed are plotted to illustrate the range of positions they can occupy. Because of the low intrinsic hardening capacity of Ti-6Al-4V, stress values at P3 are relatively uniform. However, strain values ε_3 are spread between roughly 2 % and 25 %. Stress and strain at P2 are also very scattered with stress values between 200 MPa and 800 MPa, and strain values

between 1 % and 25 %. The position of P1 reflects apparent elasticity modulus $\bar{E}$ between a few GPa and 90 GPa.

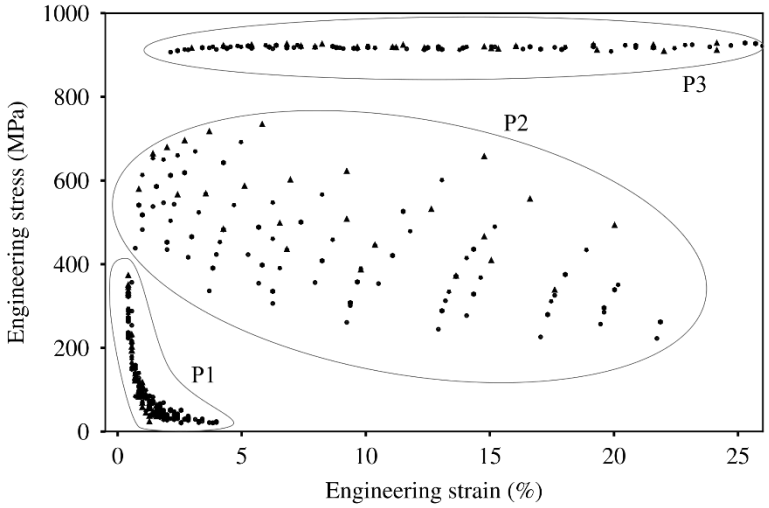

Figure 8. Position of P1, P2 and P3 for all simulations performed in which the sample reach a straight geometry within 25 % equivalent strain (i.e. P3 can be defined).

3.2. Design guidelines

Based on the characteristic points, a numerical toolbox has been established to provide input geometrical parameters (P, h and e) that would generate behaviors with specific levels of indices, in our case $\bar{E}$, H_1, H_2, ε_1, ε_2 and ε_3. The values of each index were obtained with FE simulations at multiple locations in the 3D space formed by P, h and e. Thresholding was used to delimit convex domains of this space where each index satisfied a given criterion. Design maps were then constructed to help visualize windows of potential input parameters for each target value of the indices. A selection process consisting in finding intersecting domains was used to identify potential input parameters for several cases.

Contour plots shown in Figure 9 illustrate how ε_2 depends on parameters P and h for two thicknesses (1 mm and 1.5 mm). The upper-left side of each plot is populated with simulations that lead to only a partial unbending at the end of the computation (25 % equivalent macroscopic strain). In other words, P3 could not be defined for the simulations located in that region. Some of the partial curves were related with very soft behaviors featuring a long initial plateau. Part of the simulations also reflected conditions in which actual samples were likely to fail because of high strain localization. To help visualize the area where samples are likely to fail before reaching P3 or a macroscopic strain of 25 %, a criterion was applied on the maximum local strain ε_{local} present in the field either at P3 or at the end of the simulation. An arbitrary value for the criterion was

set to twice the strain to failure, i.e. 36 %, observed during the macroscopic tensile sample.

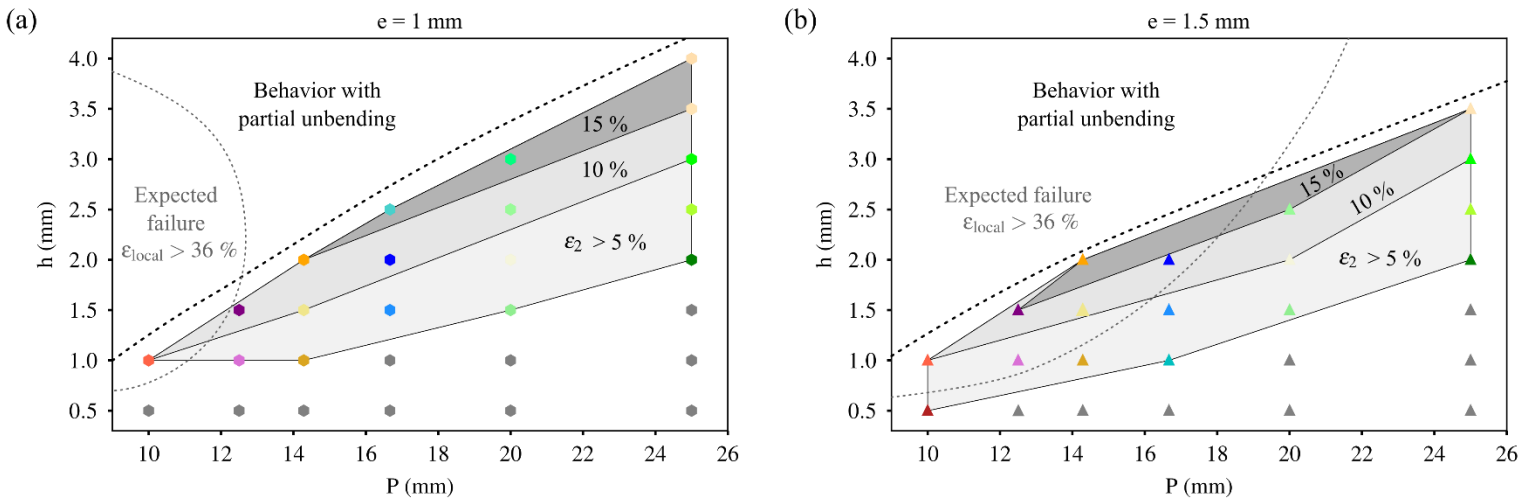

Figure 9. Predicted contour plots for ε_2 as a function of P and h. Two slices of the parameter space are shown for $e = 1\ mm$ (a) and $e = 1.5mm$ (b). The upper-left side of each plot is populated with simulations leading to partial unbending (P3 is not defined). The area of expect failure indicates geometries that are likely to fail before reaching P3 or a macroscopic strain of 25 %.

As seen in Figure 9(a), behaviors with high ε_2 are found for corrugations with a large amplitude and/or long period. Those behavior feature a long initial plateau that is favored by "soft" geometrical configurations. Figure 9(b) illustrates that the shape of the domains evolves significantly with the thickness. This evolution follows trends that also indirectly reflect a change in the curve shape and therefore are difficult to apprehend intuitively. As illustrated in Figure 10, the position and evolution of each domain strongly depends on the index considered. In contrast to ε_2, high moduli $\bar{E}$ and H_2 tend to be favored at low amplitude h and high period P.

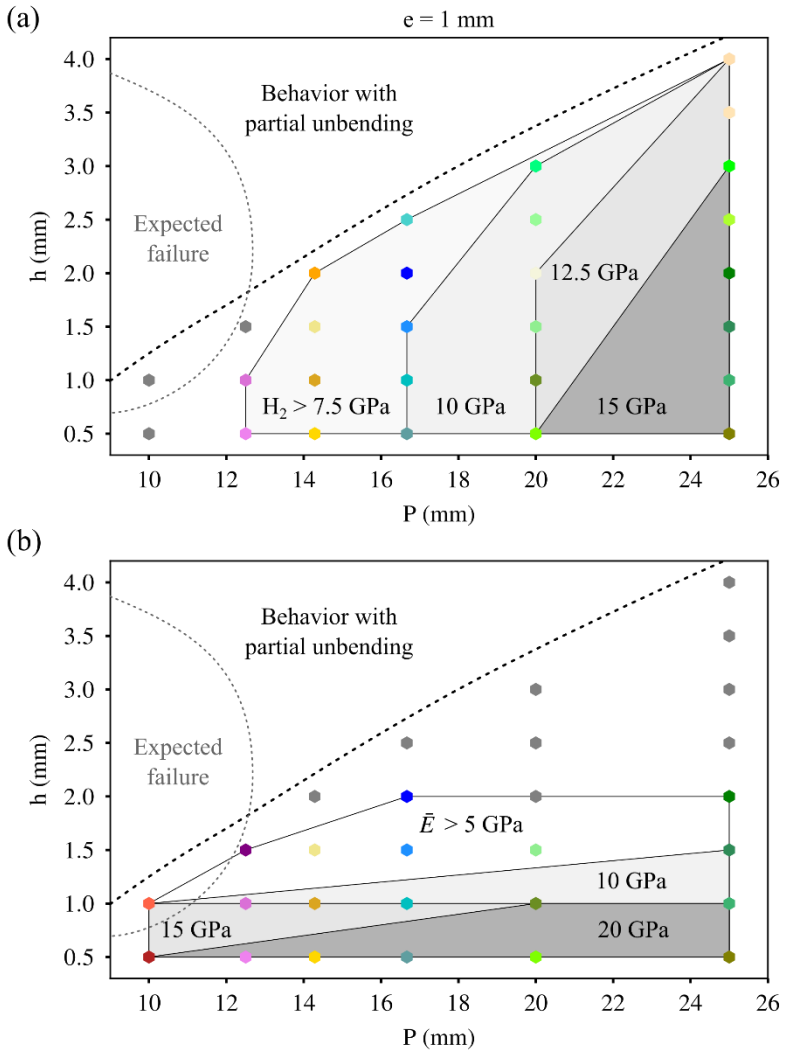

Figure 10. Predicted contour plots for descriptors H_2 (a) and $\bar{E}$ (b). The two plots are drawn for a thickness $e = 1\ mm$. The upper-left side of each plot is populated with simulations leading to partial unbending (P3 is not defined). The area of expected failure indicates geometries that are likely to fail before reaching P3 or a macroscopic strain of 25 %.

3.3. Example of a selection process

The numerical toolbox was established to answer questions such as: which geometry produces a stress-strain curve with a high Young's modulus, long plateau and high secondary hardening? Based on the toolbox a selection process was employed to design five corrugated samples with various constraints on their expected behaviors. For all samples, a target thickness of 1 mm was fixed for the sake of simplicity, even though searches can be conducted in the whole parameters space.

In a first elementary case, we searched for the geometrical parameters leading to a behavior with a long low-stress plateau. Only two solutions were found for $\varepsilon_2 > 20\ \%$ with potential input parameters being ($P = 25\ mm, h = 4\ mm$) and ($P = 16.7\ mm, h = 2.5\ mm$). The second solution was selected since the first solution

corresponded to the longest period and highest amplitude investigated by the simulations.

In a separate study, constraints were imposed on couples of indices (see Figure 11). The search was conducted to obtain behaviors with a well-formed low-stress plateau, a request first formalized with the constraint: $\varepsilon_2 > 10\ \%$. In a first case, a high equivalent Young's modulus was required ($\bar{E} > 15$ GPa). In a second case, a high secondary strain hardening was searched for ($H_2 > 16$ GPa), along with the constraint $\varepsilon_2 > 7.5\ \%$. As illustrated in Figure 11(a) and Figure 11(b), both searches yielded a single solution with ($P = 10\ mm, h = 1\ mm$) in the first case and ($P = 25\ mm, h = 2.5\ mm$) in the second case. A third case study was imagined with an opposite criterion ($\bar{E} < 30$ GPa and $\varepsilon_2 < 5\ \%$), leading to the selection of a geometry defined by ($P = 16.7\ mm, h = 1\ mm$).

In a last example, constraints were imposed on three indices. Two constraints were taken similar to the previous study ($\varepsilon_2 > 10\ \%$ and $\bar{E} > 15$ GPa) and an additional constraint was placed on the second strain hardening rate ($H_2 > 7.5$ GPa). As seen in Figure 11(c), this case illustrates a configuration where no solution was found since the three domains do not intersect. When one of the constraints was relaxed ($\bar{E} > 5$ GPa instead of $\bar{E} > 15$ GPa, see Figure 11(d)), a satisfying window of geometrical parameters was found, with for instance the satisfactory geometry ($P = 16.7\ mm, h = 2\ mm$).

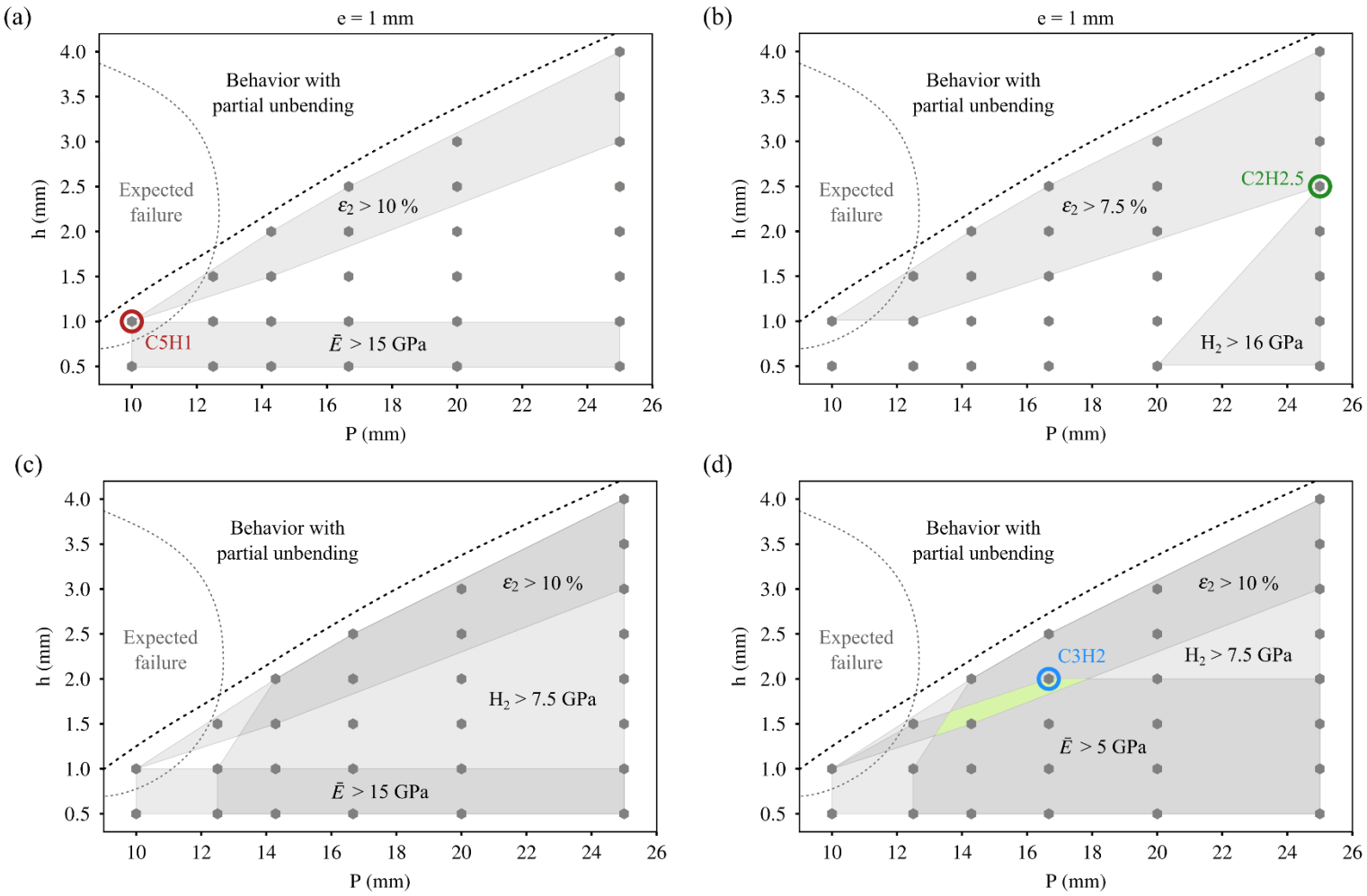

Figure 11 Design maps used to select input geometrical parameters given selected constraints on the stress-strain behavior. (a) and (b) two constrains are imposed yielding a single solution in both cases. (c) Illustration of three incompatible constrains leading to not-intersecting domains. (d) One constraint in (c) is released ($\bar{E} > 5$ GPa) leading to a window of potential input parameters.

4. Experimental validation of the *behavior by design* strategy

Five corrugated samples were built with the five geometries selected above and their experimental stress-strain response was compared with the FE model prediction. The sample characteristics measured before testing are summarized in Table 2 and several optical images of the as-built samples are shown in Figure 12. All simulations reported in this section were performed by considering the experimental thickness reported in Table 2.

Sample name	$P = L_0/c$ (mm)	h (mm)	e (mm)	w (mm)
C2H2.5	25	2.5	1.12	3.01
C3H1	16.7	1.	1.28	3.09

C3H2	16.7	2.	1.04	3.06
C3H2.5	16.7	2.5	1.01	2.83
C5H1	10	1.	1.09	2.91

Table 2. Geometrical characteristics of the corrugated tensile samples produced by additive manufacturing, before testing (i.e. after chemical etching). The notation C#H# refers respectively to the number of corrugations in the sample (c) and the amplitude (h).

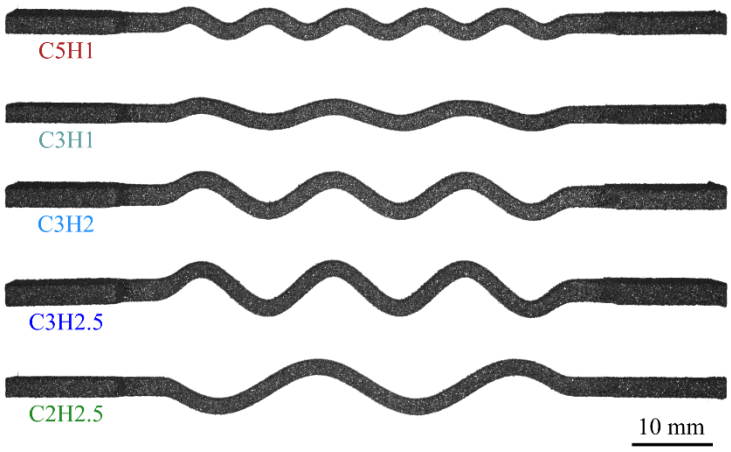

Figure 12. Optical images of the as-built Ti-6Al-4V tensile samples produced by additive manufacturing (EBM).

4.1. Experimental and simulated stress-strain responses

A comparison between experimental and simulated behaviors are shown in Figure 13. A relatively good agreement was obtained between all five couples of curves. As a general trend, the simulated behavior appears slightly shifted towards larger strain values compared to the experimental one. The mean strain difference, calculated before the high-stress plateau, is below 0.8 % for all geometries. The smallest mean distance, 0.5 %, is observed for samples C2H2.5 and C3H1. The maximum strain discrepancy, 2.1 %, is detected in the low-stress plateau of sample C3H2. When analyzing the differences in stress levels, the mean difference between the simulated and experimental curves is below 50 MPa. The largest difference measured is 120 MPa (for sample C3H2.5) but the large value is a direct consequence of the shift in strain present in the steep regions of the curve. For example, the maximum value measured on sample C5H1, which shows a progressive strain hardening, is only 41 MPa. Part of the differences in stress levels stem from the uncertainty associated with the determination of the effective cross-section used to calculate the equivalent stress level. For example, a slight underestimation of the cross-section would

explain that the peak stress of sample C2H2.5 appears higher than the plateau simulated.

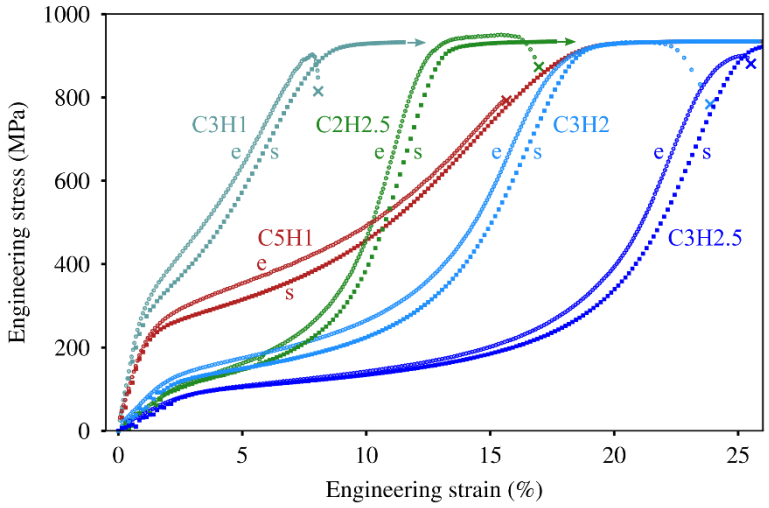

Figure 13: Comparison between simulated (s) and experimental (e) behaviors for the five corrugated samples. A cross indicates the sample failure and arrows show the high-stress plateau.

Given the good agreement between experiments and simulations, the simulated curves are used to confirm that the behaviors produced with additive manufacturing satisfy the constraints imposed in the selection process. This validation is necessary to account for the actual thickness of the samples which is different from the value $e = 1$ mm assumed during the selection process. For C3H2.5, the length of the low-stress plateau is $\varepsilon_2 = 20$ %, a value that just match the criterion of the first case study ($\varepsilon_2 > 20$ %). For C5H1, $\bar{E} = 21$ GPa and $\varepsilon_2 = 12$ % and the two values meet the criterion ($\bar{E} > 15$ GPa, $\varepsilon_2 > 10$ %). In the case of C2H2.5, $\varepsilon_2 = 9.5$ % and $H_2 = 14.6$ GPa therefore the constraint ($\varepsilon_2 > 7.5$ %) is fulfilled whereas ($H_2 > 16$ GPa) is not strictly satisfied although the observed index is close to the target value. For C3H1, $\bar{E} = 29.3$ GPa and $\varepsilon_2 = 4.7$ % so the criterion ($\bar{E} < 30$ GPa, $\varepsilon_2 < 5$ %) is met. Finally, the indices associated with C3H2 are $\bar{E} = 6.5$ GPa, $\varepsilon_2 = 13.6$ % and $H_2 = 9.7$ GPa and all values satisfy the constraints ($\bar{E} > 5$ GPa, $\varepsilon_2 > 10$ % and $H_2 > 7.5$ GPa). The results show that the numerical toolbox has been used successfully to design samples with a specific criterion on their behavior within an uncertainty of ~0.8 % strain and 50 MPa stemming from the gap observed between experimental and simulated curves.

If the simulated and experimental curves globally match for all geometries, significant differences are observed when considering the experimental behavior close to failure. Both samples C2H2.5 and C3H2 deformed significantly (~2.5 %) on the high stress plateau. Samples C3H1 and C3H2.5 localized at the beginning of the high-

stress plateau whereas sample C5H1 failed prematurely before reaching it. As illustrated in Figure 9 with an elementary criterion on the local deformation, samples with a short period (such as C5H1) are more likely to fail prematurely. Early failure is also promoted by larger thicknesses for a given corrugation, an intuitive fact that would explain why C3H1 failed earlier than a sample with the sample period and larger amplitude such as C3H2. Establishing a reliable failure criterion is a complex task not addressed in this work as it depends on both purely geometrical factors and materials-related effects such as the present of surface defects.

4.2. Impact of local shape variations on the behavior

The 3D geometry of sample C3H2 was characterized by X-ray tomography to identify local shape variations which could explain some of the differences between simulations and experiments. As shown in Figure 14(a), the sample before testing had a surface quality characteristic of previous chemical etching [25]. Chemical etching was used as a post-processing step to smooth surface defects present on the as-built surface such as stuck powder particles and plate-like defects. According to the profile of thickness presented in Figure 14(b), significant variations of thickness occur over few millimeters in the gauge section. For example, the thickness fluctuates between 1 mm to 1.1 mm in the central corrugation. A long-range variation of the thickness is also present in the sample as shown by the averaged thickness profile calculated with a moving window filter (blue line). It appears that the central corrugation is the thinnest part of the gauge section. To assess how a long-range thickness variation affects the behavior, a simulation was carried out with the profile extracted from the 3D volume. As seen in Figure 14(c), the model accounting for thickness variations provides a better representation of the experimental curve than the model with a constant thickness. The results suggest that a significant part of the gap observed previously between simulations and experiments is stemming from the simple geometry used in previous FE models. The agreement can be improved by considering local thickness variations and possibly other shape fluctuations such as small deviations from perfect sinusoidal corrugations.

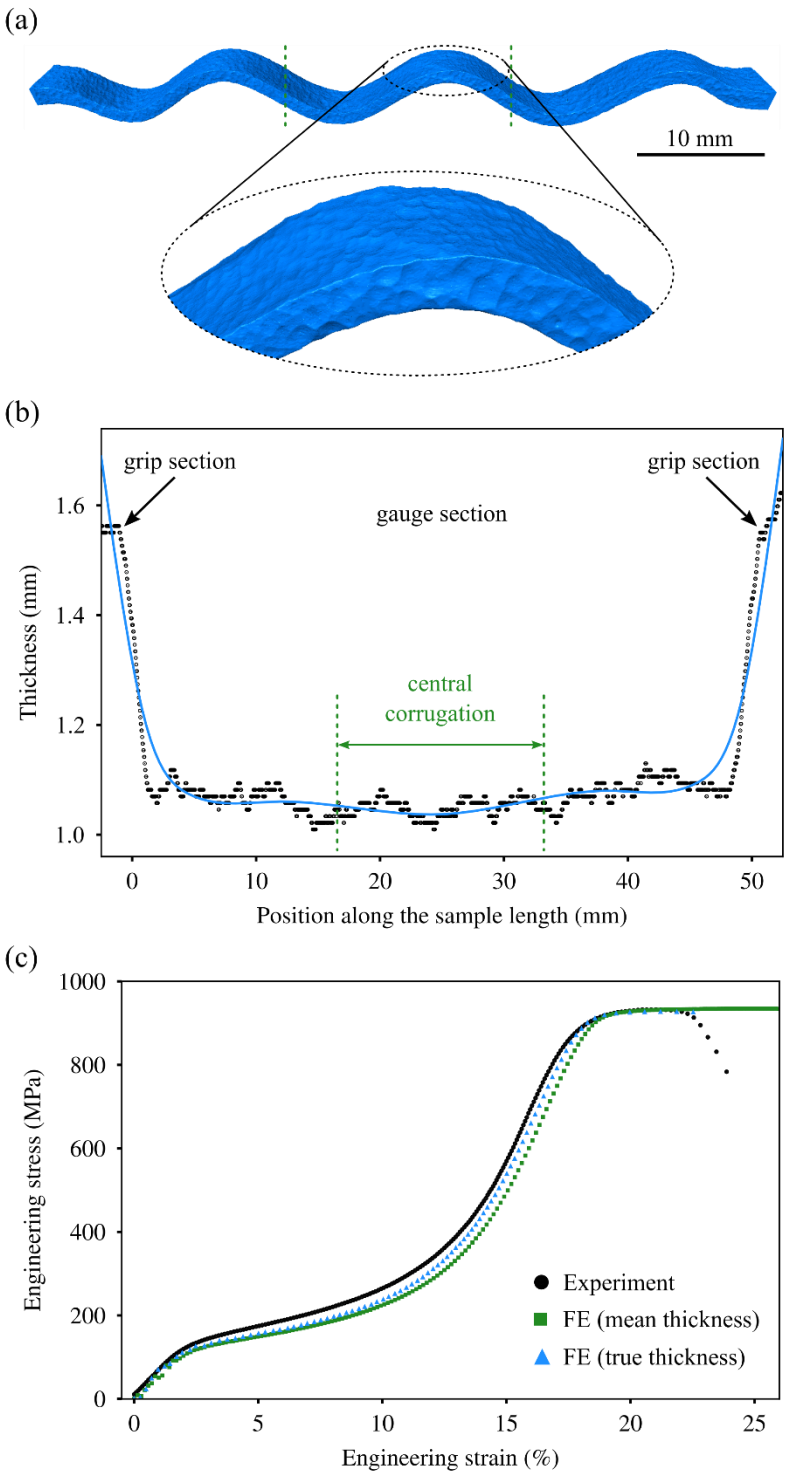

Figure 14. Characterization of the local shape variations in sample C3H2 and their impact on its behavior. (a) 3D visualization of the sample before testing. The inset present a zoomed-in region showing the surface roughness associated with chemical etching. (b) Thickness profile measured from the 3D volume (black) and the corresponding averaged profile (blue) (c) Stress-strain curves associated with the experimental behavior of C3H2 (black), the finite element model used earlier in this study (green squares) and a refined 2D model accounting for thickness variations measured by tomography (blue triangles).

5. Conclusion

A novel design strategy, referred to as *behavior by design*, was introduced to develop novel architectured materials starting from their expected stress-strain response. In the framework of corrugated tensile samples, a numerical toolbox was used to select the period *P* and the amplitude h of several corrugations leading to specific target behaviors. The toolbox was based on a finite element model which was used in a multiscale approach to construct characteristic points and indices on the macroscopic stress-strain curves. Design maps were used to illustrate the selection process carried out in the geometrical parameter space. Additive manufacturing (EBM) was employed to build the predicted geometries in Ti-6Al-4V titanium alloy. Mechanical testing revealed a good agreement between the experimental and predicted behaviors with limited differences in strain (0.8 %) and stress (50 MPa). Shape variations such as local thickness fluctuations were identified using X-ray tomography as a source of mismatch between simulations and experiments. The ability to control the whole shape of unusual stress-strain curves is expected to bring new exciting functionalities to architectured materials, especially when considering the possible extension of the concept to 3D lattice-type of architectures.

6. Acknowledgments

We gratefully acknowledge C. Josserond and X. Cerutti for their support. This work was performed within the framework of the Center of Excellence of Multifunctional Architectured Materials "CEMAM" no. AN- 10-LABX-44-01 funded by the "Investments for the Future Program".

7. Conflict of interests

The authors declare that there is no conflict of interest regarding the publication of this paper

8. Data availability

The raw/processed data required to reproduce these findings cannot be shared at this time as the data also forms part of an ongoing study.

9. References

[1] Y. Brechet, J.D. Embury, Architectured materials: Expanding materials space, Scr. Mater. 68 (2013) 1–3.

doi:10.1016/j.scriptamat.2012.07.038.

[2] M. Wang, C.C. Tasan, D. Ponge, A. Kostka, D. Raabe, Smaller is less stable : Size effects on twinning vs . transformation of reverted austenite in TRIP-maraging steels, Acta Mater. 79 (2014) 268–281. doi:10.1016/j.actamat.2014.07.020.

[3] L. Wang, J.G. Speer, Quenching and Partitioning Steel Heat Treatment, Metallogr. Microstruct. Anal. 2 (2013) 268–281. doi:10.1007/s13632-013-0082-8.

[4] F. Sun, J.Y. Zhang, M. Marteleur, T. Gloriant, P. Vermaut, D. Laillé, P. Castany, C. Curfs, P.J. Jacques, F. Prima, Investigation of early stage deformation mechanisms in a metastable β titanium alloy showing combined twinning-induced plasticity and transformation-induced plasticity effects, Acta Mater. 61 (2013) 6406–6417. doi:10.1016/j.actamat.2013.07.019.

[5] Z. Li, K.G. Pradeep, Y. Deng, D. Raabe, C.C. Tasan, Metastable high-entropy dual-phase alloys overcome the strength-ductility trade-off, Nature. 534 (2016) 227–230. doi:10.1038/nature17981.

[6] M. Ashby, Designing architectured materials, Scr. Mater. 68 (2013) 4–7. doi:10.1016/j.scriptamat.2012.04.033.

[7] T. DebRoy, H.L. Wei, J.S. Zuback, T. Mukherjee, J.W. Elmer, J.O. Milewski, A.M. Beese, A. Wilson-Heid, A. De, W. Zhang, Additive manufacturing of metallic components – Process, structure and properties, Prog. Mater. Sci. 92 (2018) 112–224. doi:10.1016/j.pmatsci.2017.10.001.

[8] X. Yu, J. Zhou, H. Liang, Z. Jiang, L. Wu, Mechanical metamaterials associated with stiffness, rigidity and compressibility: A brief review, Prog. Mater. Sci. 94 (2018) 114–173. doi:10.1016/j.pmatsci.2017.12.003.

[9] T. Tancogne-Dejean, A.B. Spierings, D. Mohr, Additively-manufactured metallic micro-lattice materials for high specific energy absorption under static and dynamic loading, Acta Mater. 116 (2016) 14–28. doi:10.1016/j.actamat.2016.05.054.

[10] O. Bouaziz, Geometrically induced strain hardening, Scr. Mater. 68 (2013) 28–30. doi:10.1016/j.scriptamat.2012.08.008.

[11] M. Fraser, H. Zurob, P. Wu, O. Bouaziz, Analytical model of the unbending behavior of corrugated reinforcements, Adv. Eng. Mater. 16 (2014) 872–877. doi:10.1002/adem.201300525.

[12] M. Fraser, STUDY OF ARCHITECTURED MATERIALS WITH A CORRUGATED, McMaster University, 2017.

[13] A. Ataee, Y. Li, D. Fraser, G. Song, C. Wen, Anisotropic Ti-6Al-4V gyroid scaffolds manufactured by electron beam melting (EBM) for bone implant applications, Mater. Des. 137 (2018) 345–354. doi:10.1016/j.matdes.2017.10.040.

[14] E. Hernández-Nava, C.J. Smith, F. Derguti, S. Tammas-Williams, F. Leonard, P.J. Withers, I. Todd, R. Goodall, The effect of defects on the mechanical response of Ti-6Al-4V cubic lattice structures fabricated by electron beam melting, Acta Mater. 108 (2016) 279–292. doi:10.1016/j.actamat.2016.02.029.

[15] O. Cansizoglu, O. Harrysson, D. Cormier, H. West, T. Mahale, Properties of Ti-6Al-4V non-stochastic lattice structures fabricated via electron beam melting, Mater. Sci. Eng. A. 492 (2008) 468–474. doi:10.1016/j.msea.2008.04.002.

[16] L.E. Murr, S.M. Gaytan, F. Medina, E. Martinez, J.L. Martinez, D.H. Hernandez, B.I. Machado, D.A. Ramirez, R.B. Wicker, Characterization of Ti-6Al-4V open cellular foams fabricated by additive manufacturing using electron beam melting, Mater. Sci. Eng. A. 527 (2010) 1861–1868. doi:10.1016/j.msea.2009.11.015.

[17] O.L.A. Harrysson, O. Cansizoglu, D.J. Marcellin-Little, D.R. Cormier, H.A. West, Direct metal fabrication of titanium implants with tailored materials and mechanical properties using electron beam melting technology, Mater. Sci. Eng. C. 28 (2008) 366–373. doi:10.1016/j.msec.2007.04.022.

[18] N. Hrabe, T. Quinn, Effects of processing on microstructure and mechanical properties of a titanium alloy (Ti-6Al-4V) fabricated using electron beam melting (EBM), Part 2: Energy input, orientation, and location, Mater. Sci. Eng. A. 573 (2013) 271–277. doi:10.1016/j.msea.2013.02.065.

[19] C. de Formanoir, S. Michotte, O. Rigo, L. Germain, S. Godet, Electron beam melted Ti-6Al-4V: Microstructure, texture and mechanical behavior of the as-built and heat-treated material, Mater. Sci. Eng. A. 652 (2016) 105–119. doi:10.1016/j.msea.2015.11.052.

[20] X. Zhao, S. Li, M. Zhang, Y. Liu, T.B. Sercombe, S. Wang, Y. Hao, R. Yang, L.E. Murr, Comparison of the microstructures and mechanical properties of Ti-6Al-4V fabricated by selective laser melting and electron beam melting, Mater. Des. 95 (2016) 21–31. doi:10.1016/j.matdes.2015.12.135.

[21] T. Persenot, A. Burr, G. Martin, J.-Y. Buffiere, R. Dendievel, E. Maire, Effect of build orientation on the fatigue properties of as-built Electron Beam Melted Ti-6Al-4V alloy, Int. J. Fatigue. 118 (2018) 65–76. doi:10.1016/j.ijfatigue.2018.08.006.

[22] S. Tammas-Williams, P.J. Withers, I. Todd, P.B. Prangnell, The Effectiveness of Hot Isostatic Pressing for Closing Porosity in Titanium Parts Manufactured by Selective Electron Beam Melting, Metall. Mater. Trans. A Phys. Metall. Mater. Sci. 47 (2016) 1939–1946. doi:10.1007/s11661-016-3429-3.

[23] S. Tammas-Williams, P.J. Withers, I. Todd, P.B. Prangnell, Porosity regrowth during heat treatment of hot isostatically

pressed additively manufactured titanium components, Scr. Mater. 122 (2016) 72–76. doi:10.1016/j.scriptamat.2016.05.002.

[24] M. Suard, G. Martin, P. Lhuissier, R. Dendievel, F. Vignat, J.J. Blandin, F. Villeneuve, Mechanical equivalent diameter of single struts for the stiffness prediction of lattice structures produced by Electron Beam Melting, Addit. Manuf. 8 (2015) 124–131. doi:10.1016/j.addma.2015.10.002.

[25] P. Lhuissier, C. de Formanoir, G. Martin, R. Dendievel, S. Godet, Geometrical control of lattice structures produced by EBM through chemical etching: Investigations at the scale of individual struts, Mater. Des. 110 (2016) 485–493. doi:10.1016/j.matdes.2016.08.029.

[26] C. de Formanoir, M. Suard, R. Dendievel, G. Martin, S. Godet, Improving the mechanical efficiency of electron beam melted titanium lattice structures by chemical etching, Addit. Manuf. 11 (2016) 71–76. doi:10.1016/j.addma.2016.05.001.

[27] T. Persenot, G. Martin, R. Dendievel, J.Y. Buffiére, E. Maire, Enhancing the tensile properties of EBM as-built thin parts: Effect of HIP and chemical etching, Mater. Charact. (2018) 1–12. doi:10.1016/j.matchar.2018.01.035.